



Combining Dynamic Monte Carlo with Machine Learning to Study Nanoparticle Translocation

Journal:	<i>Soft Matter</i>
Manuscript ID	SM-ART-04-2022-000431.R1
Article Type:	Paper
Date Submitted by the Author:	13-Jun-2022
Complete List of Authors:	Vieira, Luiz ; Case Western Reserve University, Department of Macromolecular Science and Engineering Weinhofer, Alexandra; Case Western Reserve University, Macromolecular Science and Engineering Oltjen, William; Case Western Reserve University, Macromolecular Science and Engineering Yu, Cindy; Hathaway Brown School de Souza Mendes, Paulo; Pontifícia Universidade Católica - RJ, Mechanical Engineering Hore, Michael; Case Western Reserve University, Macromolecular Science and Engineering

Cite this: DOI: 00.0000/xxxxxxxxxx

Combining Dynamic Monte Carlo with Machine Learning to Study Nanoparticle Translocation[†]

Luiz Fernando Vieira^{a,b,c}, Alexandra C. Weinhofer^a, William C. Oltjen^a, Cindy Yu^d, Paulo Roberto de Souza Mendes^b, and Michael J. A. Hore,^{*‡a}

Received Date

Accepted Date

DOI: 00.0000/xxxxxxxxxx

Resistive pulse sensing (RPS) measurements of nanoparticle translocation have the ability to provide information on single-particle level characteristics, such as diameter or mobility, as well as ensemble averages. However, interpreting these measurements is complex and requires an understanding of nanoparticle dynamics in confined spaces as well as the ways in which nanoparticles disrupt ion transport while inside a nanopore. Here, we combine Dynamic Monte Carlo (DMC) simulations with Machine Learning (ML) and Poisson-Nernst-Planck calculations to simultaneously simulate nanoparticle dynamics and ion transport during hundreds of independent particle translocations as a function of nanoparticle size, electrophoretic mobility, and nanopore length. The use of DMC simulations allowed us to explicitly investigate the effects of Brownian motion and nanoparticle/nanopore characteristics on the amplitude and duration of translocation signals. Simulation results were verified with experimental RPS measurements and found to be in quantitative agreement.

1 Introduction

Translocation can be described as the passage of nanoscale objects through confined spaces, such as nanopore or nanochannel. This phenomenon is not only important in processes such as filtering¹ and viral infection², but also can be used as a characterization tool. As a characterization tool, the nano-objects are dispersed in an electrolyte solution and placed into a flow cell with two chambers separated by a membrane containing one or more nanopores. When a difference of electrical potential is applied between the two sides of the cell, an ionic current on the order of picoamperes to nanoamperes can be measured. As the object translocates from one side of the cell to the other, it affects the flow of ions. Typically, the object decreases the flow of ions indicated by a pulse in the current measurement, and the technique is referred to as resistive pulse sensing (RPS). However, for certain types of nanoparticles, such as citrate-coated Au nanoparticles, it is possible to observe conductive pulses corresponding to

an increase in the flow of ions through the channel. Conductive pulses have been attributed to the structure of the surface coating.^{3–5} By the analysing descriptors of the pulse that occurs as a result of the object moving through the pore, one can infer the properties of the object.

Nanopore sensing initially attracted the attention of researchers as a promising DNA sequencing platform. In addition to that, nanopore sensing is regarded as a feasible technique with which to characterize nanoparticles due its ability to measure physical properties at a single particle level, unlike with techniques such as dynamic light scattering (DLS), and with high-throughput, unlike with traditional electron microscopy. Average values corresponding to the ensemble of objects can be obtained by analyzing the results of many translocation events. Experimental translocation measurements have successfully studied polymeric and inorganic spheres^{6–44}, rods^{41,44}, cuboids⁴⁵, vesicles^{9–11,46–49} and virus-like particles.^{20,29,50–58} In particular, it has been successful in characterizing the size^{6,9,13,15,20,21,26,27,29,32,34–36,48,54,57–61}, surface charge^{5,6,13,15,21,26,32,36,41,57,58,61} and concentration^{32,33,35,54} of particles with submicrometer sizes. The stiffness of soft particles with these techniques has also been studied.^{49,62,63}

Despite advances in hardware⁶⁴ and data treatment^{6,50,65}, it can be challenging to establish unequivocal relations between the current pulses that are measured and the properties of interest. Modeling and simulation techniques are very important tools to help unveil the complex phenomena present during the

^a Department of Macromolecular Science & Engineering, Case Western Reserve University, 10900 Euclid Avenue, Cleveland, OH 44106, USA. E-mail: hore@case.edu; Tel: +1 216 368 0793

^b Department of Mechanical Engineering, Pontifícia Universidade Católica do Rio de Janeiro, Rua Marquês de São Vicente 225, Rio de Janeiro, RJ 22451-900, Brazil

^c Instituto Nacional de Tecnologia, Ministry of Science, Technology & Innovation, Av. Venezuela, 82 - Rio de Janeiro, RJ 20081-312, Brazil.

^d Hathaway Brown School, 19600 North Park Blvd., Shaker Heights, OH 44122, USA.

[†] Electronic Supplementary Information (ESI) available: [details of any supplementary information available should be included here]. See DOI: 10.1039/cXsm00000x/

translocation. To this end, several simulation methods have been used successfully to understand aspects of particle translocation. Langevin Dynamics simulations were utilized to study the capture⁶⁶, entrance and translocation^{53,57,67} of slightly flexible, anisotropic particles, such as the Tobacco Mosaic Virus (TMV) viral capsid. Additionally, Monte Carlo simulation schemes were also used to explore the capture radius⁶⁸ and diffusivity of a particle under confinement.⁶⁹ Finally, Lattice Boltzmann simulations have been developed to deal with the electrokinetic problem⁷⁰ and were used to study the translocation of a double helix of DNA.⁷¹ The majority of the literature on this topic, however, has relied on simulations using the Finite Element Method (FEM).^{5,6,14,16,19,25,27,28,30,47,62,72–76}

When trying to relate particle properties with the current signal, each particle position in its trajectory usually represents a single simulation run. Most of the studies consider either a single, unique simulation with the particle at the center of the pore or a collection of runs with particles placed within a straight line trajectory. For example, Tsutsui *et al.*¹⁶ observed distinct populations of current signals while investigating polystyrene latex particles translocating through low aspect ratio pores. FEM simulations of particles in different positions along the pore indicate trajectory-dependent currents, notably due to off-axis displacement of the particles. The authors performed cross-sectional (2D) Brownian Dynamics simulations to investigate degree of temporal fluctuations in the particle center position due to Brownian motion. They state, however, that “*simultaneous simulation of the particle dynamics and the ion transport would shed further light on this intriguing phenomenon*”.¹⁶

Motivated by this body of prior work, in this paper we propose a procedure to simulate simultaneously the drift-diffusion trajectories and the current response to these trajectories using Dynamic Monte Carlo simulations that are coupled to a machine-learning approach to calculating the electrostatic potential and ionic current through the nanopore. To accomplish this, first the electrostatic potential and ionic current are solved for several configurations of pore/particle properties and particle position. These results are used to train neural networks that capture the input-output relationship between particle position and electrostatic potential. Finally, Dynamic Monte Carlo is used to compute time-resolved trajectories and map the ionic current related to each position for a large ensemble of particles. By simulating several configurations of particle diameter, particle mobility and pore length, we show how the thermal fluctuations can affect the resolution and robustness of the measurements. Finally, we compare our calculations to experimental translocation measurements and show that the DMC simulations are in quantitative agreement with experiments.

2 Methods

2.1 Poisson-Nernst-Planck (PNP) Framework

The electrostatic potential and ionic current through the nanopore were calculated using the Poisson-Nernst-Planck (PNP) formalism. In this approach, the electrostatic potential is obtained by solving the Poisson equation, and the solution is then used

to solve the Nernst-Planck equation for the ion concentrations and fluxes throughout the system. The process is performed self-consistently until the error falls below a desired threshold. For our calculations, the process was repeated until the error in the electrostatic potential and ion concentrations fell below 10^{-7} V and 10^{-6} mol L⁻¹, respectively. The calculations were performed on a cubic system with $L_x = L_y = L_z = 500$ nm, with each dimension discretized into 128 grid points. This resulted in a spatial resolution of $\Delta x = \Delta y = \Delta z \approx 4$ nm. The PNP equations were solved using an in-house code written in C++ using the NVIDIA CUDA libraries, and the calculations performed on NVIDIA Tesla P100 and V100 GPUs.

Within the PNP framework, the electrostatic potential throughout the system, $\phi(\mathbf{r})$, is first calculated by solving the Poisson equation:

$$\nabla \cdot [\epsilon_r(\mathbf{r}) \nabla \phi(\mathbf{r})] = -\frac{\rho_m(\mathbf{r})}{\epsilon_0} \quad (1)$$

where $\epsilon_r(\mathbf{r})$ is the relative permittivity at position \mathbf{r} in the system, $\rho_m(\mathbf{r})$ is the mobile charge density at that position, and ϵ_0 is the permittivity of free space. Regions belonging to the solution have $\epsilon_r(\mathbf{r}) = 80$ while regions inside the membrane or nanoparticle have $\epsilon_r(\mathbf{r}) = 2$. The Poisson equation was solved using a successive over-relaxation (SOR) algorithm with the boundary conditions that $\phi(\mathbf{r}) = V_b = 100$ mV at $z = 500$ nm, and $\phi(\mathbf{r}) = 0$ mV at $z = 0$ nm. The initial condition for $\phi(\mathbf{r})$ was $\phi(\mathbf{r}) = 0$ throughout the system, except at the boundaries. We simulated a single membrane with thickness L_p , containing a cylindrical nanopore with diameter $d_p = 60$ nm, centered in the system, and oriented perpendicular to the xy -plane of the system. For simplicity, the nanoparticle and membrane were modeled as uncharged surfaces.

The electrostatic potential was then used to solve the Nernst-Planck equation:

$$\nabla \cdot \left[D_i \nabla c_i(\mathbf{r}) + \frac{D_i Z_i}{k_B T} c_i(\mathbf{r}) \nabla \phi \right] = 0 \quad (2)$$

where D_i and $c_i(\mathbf{r})$ are the diffusion coefficients and concentrations, respectively, of ion i , and Z_i is the charge carried by the ion. The Nernst-Planck equation was solved using SOR after being cast into a more convenient form with a Slotboom transformation.⁷⁷ To mimic our experimental system which uses a KCl electrolyte solution, we used $D_{K^+} = 1.96 \times 10^5$ cm² s⁻¹ and $D_{Cl^-} = 2.03 \times 10^5$ cm² s⁻¹, and the equilibrium concentrations of both ions were set to 0.1 mol L⁻¹. The concentrations calculated from the Nernst-Planck equation were used to construct refined values of $\rho_m(\mathbf{r})$, which were used to refine the electrostatic potential.

Finally, the ionic current for both species was calculated from their flux $\mathbf{j}_i(\mathbf{r})$, where

$$\mathbf{j}_i(\mathbf{r}) = -D_i \left[\nabla c_i(\mathbf{r}) + \frac{Z_i c_i(\mathbf{r})}{k_B T} \nabla \phi(\mathbf{r}) \right] \quad (3)$$

and the current in the z -direction, through the nanopore is calcu-

lated as

$$i(z) = \frac{2F}{L_z} \int_{\frac{L_z}{2}-\frac{L_p}{2}}^{\frac{L_z}{2}} \int_0^{L_x} \int_0^{L_y} [\mathbf{j}_{K^+}(\mathbf{r}) + \mathbf{j}_{Cl^-}(\mathbf{r})] \cdot \hat{\mathbf{z}} \, dx dy dz \quad (4)$$

where F is Faraday's constant. In principle, calculating the current from the charge flux at a single position z of the grid across the pore would be sufficient to characterize response of the ionic current to the presence of a nanoparticle. However, due to the finite size of the grid, we observed slight variations of the current at different values of z . To minimize the influence of such variations on our results, we choose to average $i(z)$ across a thicker region of space in the bottom half of the pore: $z \in [L_z/2 - L_p/2, L_z/2]$.

2.2 Machine Learning (ML)

Even with the enhancements in computational performance achieved by using GPUs, PNP calculations take several minutes to converge, effectively making them incompatible with Monte Carlo simulations that would require a PNP calculation for each trial move. To address this challenge, a neural network was used to model the results from a representative training set of PNP calculations, resulting in an accurate estimation of the electrostatic potential and ionic current for a given nanoparticle position that could be calculated within a few milliseconds.

Although there are many options for the neural network, we chose to use a multilayer perceptron (MLP) neural network due to the simplicity of its implementation and the usefulness of MLPs as universal function approximators.

MLPs are feedforward networks. The first (input) layer uses the particle position as input and the next each layer uses the previous layer as input, modified by the activation function. Rectified Linear Units (ReLU) were used as activation functions for all layers except the output layer which used a unit linear function. Therefore, the values in the neurons of each layer a_n were calculated as:

$$a_n = f_n W_n a_{n-1} \quad (5)$$

where f_n is the activation function for layer n , W_n is a matrix with the weights and bias for layer n , and a_{n-1} is the layer input.

The final neural network architecture was composed of one input layer, 5 hidden layers with 50 neurons each and one output layer containing a single neuron that carries the value of the predicted electrostatic potential. The representation of the MLP structure is shown in Figure S4 of the ESI†. The justification for this choice of the network architecture is presented below, but briefly, was the result of choosing the smallest number of layers and neurons which can reliably reproduce the PNP results. Although we chose to train the MLP to predict the electrostatic potential as a function of the nanoparticle location, alternative approaches such as training it to predict the perturbation in the electrostatic potential due to the presence of the nanoparticle could also be used.

The MLP was trained in python with Tensorflow/Keras, using the Adam optimizer algorithm, mean squared error as the loss metric validation, a split of 0.1 for the training set, a number of epochs of 1000, and batch size of 256. Additionally, a variable

learning rate was used with initial value of 0.01 and 50% decay at each 100 epochs. The optimized weights and biases were recorded in a text file that was read by the Dynamic Monte Carlo simulation code. A sample PNP data file and a python script showing the implementation/training of the MLP is freely available at https://github.com/mjahore/Translocation_NN.

2.3 Dynamic Monte Carlo (DMC)

Colloidal particles in suspension have stochastic trajectories due to the influence of thermal fluctuations. We used Metropolis Monte Carlo (MC) to mimic these fluctuations and simulate the trajectories of nanoparticles as they translocated through a nanopore.

For each Monte Carlo step, a random translation of a nanoparticle is attempted and either rejected or accepted according to the Metropolis algorithm. In this approach, the energy of old and new configurations are calculated and compared. If there is a decrease in energy, the trial is always accepted; otherwise, if the energy increases the new configuration is accepted with a probability depending on the Boltzmann factor of the increase in energy. The probability is given by:

$$p(\Delta U) = \begin{cases} 1 & \Delta U \leq 0 \\ e^{-\beta \Delta U} & \Delta U > 0 \end{cases} \quad (6)$$

If a trial move results in overlap between the particle and the membrane, then $\Delta U = \infty$ and the move is rejected. The potential energy U was calculated by the product of the electrostatic potential and the effective charge. Contained in Section 3 of the Electronic Supplementary Information (ESI†) is a detailed analysis of the particle mobility in DMC simulations. This analysis confirms the correct implementation of the DMC simulations and also provides an analytical expression for finding the effective charge needed to result in a desirable particle mobility.

The electrostatic potential was calculated by running the trained neural network implemented within the DMC code. The current through the pore for each nanoparticle position was calculated by linear interpolation from the tabulated values calculated by PNP.

Although the use of Metropolis Monte Carlo to mimic Brownian motion is not new⁷⁸, Cuetos and Pati^{79,80} recently developed an alternative DMC algorithm that directly links the Monte Carlo steps to a unique time-scale that depends on diffusion coefficient of the particles. The intrinsic MC time step is given by:

$$\delta t_{MC} = \frac{(\delta_{\mathbf{x}}^{max})^2}{2D} \quad (7)$$

where D is the diffusion coefficient obtained from the Stokes-Einstein relation:

$$D = \frac{k_B T}{3\pi\eta d_{NP}} \quad (8)$$

A time step that is equivalent to a Brownian dynamics simulation is calculated from the intrinsic (MC) time step corrected by the acceptance rate:

$$\delta t = \frac{\overline{\mathcal{A}}}{3} \times \delta t_{MC} \quad (9)$$

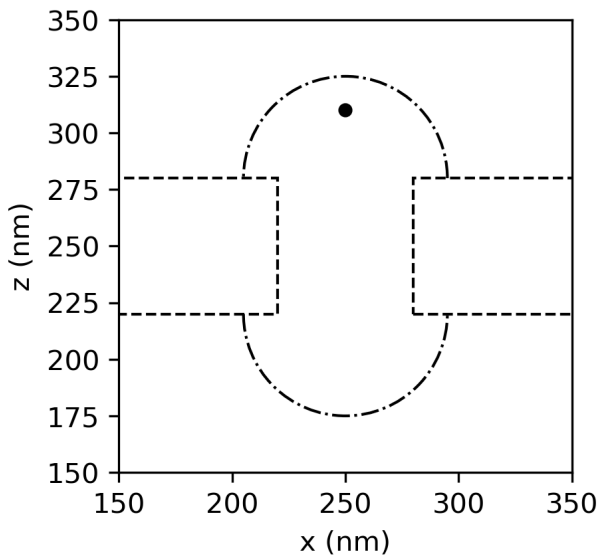


Fig. 1 Schematic of the boundary conditions used in the DMC simulation. Dotted lines represent the membrane/pore location, whereas the dash-dotted lines indicate the boundaries where the trajectories are terminated. The black dot indicates the particle's initial position.

where $\overline{\mathcal{A}}$ is defined as:

$$\overline{\mathcal{A}} = \frac{\text{Accepted trials}}{\text{Total steps}} \quad (10)$$

To improve computational efficiency we implemented the boundary condition depicted in the figure 1. The particle is initiated in the upper half of the (3D) box aligned with the main axis of the pore, at a height of $r_p = d_p/2$ above the membrane surface. The particle at this location causes only a very slight decrease in ionic current, as will be discussed later.

The dash-dotted lines denotes the boundary of an access region within a factor of 1.5 of radius of the pore entrance and exit, where most part of the field decays to very low values⁸¹ and the relative blockade is negligible. When a particle reaches one of the two “caps”, the event is terminated, the particle is re-initiated in the central axis and a new trajectory of a new event is recorded.

For most of the simulations, we fixed the applied voltage $V = 100$ mV and pore diameter $d_p = 60$ nm, and varied the pore length L_p , particle diameter d_{NP} and particle mobility μ_{NP} . A direct comparison with an experimental measurement was simulated considering $d_{NP} = 30$ nm, $d_p = 80$ nm, $L_p = 100$ nm, and particle mobility $\mu_{NP} = 0.25 \mu\text{m cm} / \text{V} \cdot \text{s}$ with an applied voltage of $V = 200$ mV.

2.4 Experimental Methods

Experimental translocation measurements were performed on cetyltrimethyl ammonium bromide (CTAB)-coated Au nanospheres (Nanopartz Inc., Loveland, CO), with average diameters of $d_{NP} = 30$ nm. The particles were dispersed in a 0.500 mol L^{-1} KCl electrolyte solution at a concentration of $\phi_{NP} = 9.2 \times 10^{10}$ NPs/mL. Low-noise SiO_2 -supported SiN_x membranes ($L_p = 100$ nm), containing a single $d_p = 80$ nm nanopore, were purchased

from Goeppert, Inc. (Philadelphia, PA). The membranes were cleaned in hot Piranha solution (3:1 mixture by volume of H_2SO_4 to 30% H_2O_2 , $T = 80$ °C) for 10 minutes, rinsed with Milli-Q water, and stored in isopropyl alcohol prior to use. **Caution:** Piranha solution is a highly corrosive and energetic solution, and should be handled with extreme care.

Ionic current measurements were performed using an eNPR amplifier (Elements srl, Cesena, Italy) equipped with a 2nd generation Elements flow cell and Ag/AgCl electrodes. The ionic current through the nanopore was sampled at a frequency of 200 kHz, resulting in a final bandwidth of 20 kHz after applying a low-pass filter to remove high frequency noise, limiting temporal resolution to approximately $50 \mu\text{s}$. Ag/AgCl electrodes were fabricated by exposing Ag wire to a 7.4% sodium hypochlorite solution for 10 minutes. Prior to measuring nanoparticle translocations, proper wetting of the nanopore by the electrolyte was verified by measuring the resistance and capacitance of the membrane. Afterwards, the nanoparticle solution was loaded into the *cis*-chamber of the flow cell, and electrolyte solution into the *trans*-chamber. A potential difference of 200 mV was applied across the chamber and the ionic current monitored for approximately 10 minutes. Translocation events were extracted and analyzed with the Pypore software package (<https://github.com/parkin/pypore>).

3 Results and Discussion

3.1 Neural Network Training with PNP

Before investigating nanoparticle translocation with DMC simulations, we performed PNP calculations to determine the electrostatic potential and ionic current for a series of imposed nanoparticle positions, which formed a set of training data for our neural network. A new neural network was trained for each value of nanoparticle and/or nanopore diameter. Figure 2a shows a slice of the electrostatic potential in the xz -plane for $y = 250$ nm in the open pore configuration without a nanoparticle present. The dashed lines in the figure indicate the position of the membrane which contains the nanopore. In all of the PNP calculations, the largest amount of variation in the electrostatic potential occurs in the region of the system containing the membrane, in agreement with the literature.⁸² Results for all three pore diameters used in this study are shown in the ESI.†

When a nanoparticle is placed in the nanochannel it influences the electrostatic potential nearby. However, as both particle and membrane are treated as uncharged surfaces in our PNP calculations, the potential at the center of the particle is the same as the potential calculated in the open pore. In figure 2b, we show the difference between the electrostatic potential with and without a nanoparticle in the center. Far from the membrane, we find that the electrostatic potential is essentially unchanged when a nanoparticle is present in the pore. However, near the nanoparticle, the electrostatic potential immediately above and below the particle can vary as much as ± 10 mV relative to the open pore for the parameters that we investigated.

To mimic real particle translocation events, the effect of the particle position on the current was investigated for several off-

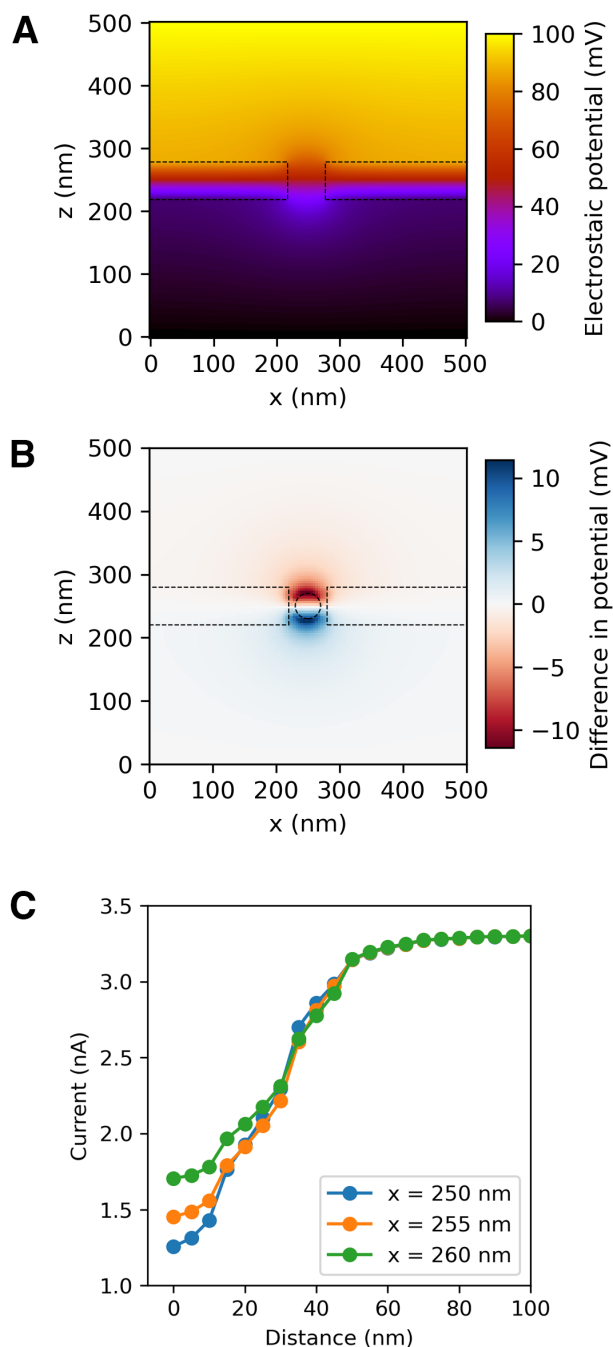


Fig. 2 (a) Electrostatic potential in the xz -plane for $y = 250$ nm. The dashed lines denote the boundaries of the membrane. (b) Difference in electrostatic potential between the open pore configuration, shown in (a), and a pore containing a $d_{NP} = 40$ nm nanoparticle in the center at $x = z = 250$ nm. (c) Current as a function of distance for three straight trajectories along the z -direction of the nanopore ($d_p = 60$ nm, $L_p = 60$ nm). A distance of 0 nm corresponds to the position $z = 250$ nm. As the particle is offset in increments of 5 and 10 nm ($x = 255$ nm and 260 nm, respectively) from the central axis of the nanopore ($x = 250$ nm), the minimum current increases implying that fewer ions are blocked by the particle. The nanoparticles in these simulations had diameters of $d_{NP} = 40$ nm and mobilities of $\mu_{NP} = 0.8 \mu\text{m cm/V}\cdot\text{s}$.

axis positions. These data confirm that setting the initial particle position *ca.* 100 nm away from the mid-point of the nanopore does not significantly impact the ionic current. Indeed, the presence of the nanoparticle only begins to affect the value of the ionic current when it is within approximately 10 nm of the entrance regardless of the amount the particle is offset from the nanopore's central axis. Previous work^{16,72} has found that off-axis positions of the nanoparticle lead to higher values of the blockade current than for nanoparticles in the center of the pore, and that this effect becomes more prominent as the pore length decreases. The origin of the increased blockade currents is due to an increase in the resistance attributed to non-uniformities in the electric field that occur for off-axis nanoparticle positions. Figure 2c shows the values of the ionic current as a function of a $d_{NP} = 40$ nm particle's position within a 60 nm diameter pore (z) in z for three values of the x -position: one at the central axis of the pore ($x = 250$ nm, blue circles) and two positions that are offset by 5 nm ($x = 255$ nm, orange circles) and 10 nm ($x = 260$ nm, green circles). The full set of results used to train the neural network are provided in the ESI†. Unlike previous calculations¹⁶, we find that off-axis positions result in smaller blockades. However, our calculations are performed at ionic strengths which are orders of magnitude larger than those previous calculations, making a direct comparison difficult. Nevertheless, using ion resistivities of $\rho_{K^+} = 1.36 \times 10^9 \Omega \cdot \text{nm}$ and $\rho_{Cl^-} = 1.31 \times 10^9 \Omega \cdot \text{nm}$, we estimate total ionic current through the pore due to the combination of resistance inside the pore and the access resistance as:

$$i_0 = \frac{\pi V_b d_p^2}{(4L_p + \pi d_p)} \left[\frac{1}{\rho_{K^+}} + \frac{1}{\rho_{Cl^-}} \right] \quad (11)$$

where $V_b = 100$ mV is the applied bias. The above expression predicts $i_0 \approx 2.9$ nA, compared to $i_0 \approx 3.2$ nA produced from our PNP calculations. Thus, our PNP calculations are in near quantitative agreement with the expected ionic current through the pore. As expected, as the nanoparticle moves deeper into the pore (i.e., as distance decreases in figure 2c), the ionic current decreases due to blockage by the particle.

A subset of PNP results were used to train the MLP neural network (NN), and its predictions were compared to a separate set of PNP calculations to assess the accuracy of the predictions as a function of the NN architecture. The difference between the PNP calculation and NN predictions is shown in figure 3 for 2, 6, and 10 layers of neurons (rows, left to right) containing 10, 50, and 100 neurons in each layer (columns, top to bottom). Perfect agreement between PNP and the MLP NN would be indicated by an absence of color. We observe that the minimum number of layers and neurons per layer that accurately reproduce the electrostatic potential in the membrane occurs for 6 layers of 50 neurons, and that the accuracy of the NN prediction increases with both increasing numbers of layers and/or an increase in the number of neurons per layer. Thus, we chose to use a NN with 6 layers that contain 50 neurons in each layer to avoid over-fitting the PNP data.

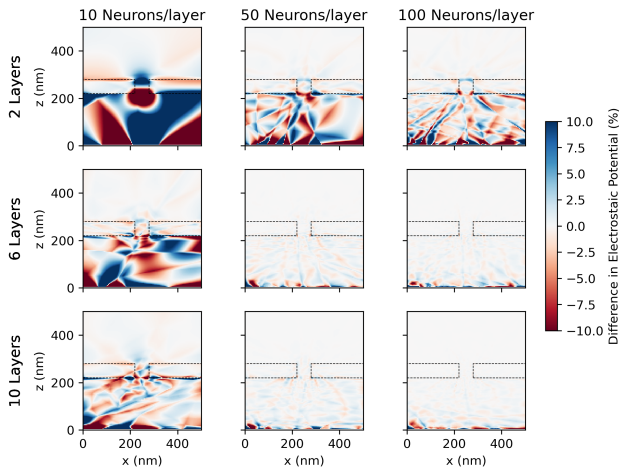


Fig. 3 Difference between the electrostatic potential calculated by PNP and predicted by the neural network for a nanopore with diameter $d_p = 60$ nm and length $L_p = 60$ nm for (top to bottom) 2, 6, and 10 layers in the network, and for (left to right) 10, 50 and 100 neurons per layer. The dashed line denotes the position of the membrane. For all NN configurations, the nanoparticle diameter was fixed at $d_{NP} = 40$ nm.

3.2 Dynamic Monte Carlo (DMC)

DMC simulations were performed for three values of nanopore length ($L_p = 20, 60,$ and 100 nm) and three values of nanoparticle diameter ($d_{NP} = 30, 40,$ and 50 nm). In all simulations, the nanopore diameter was fixed at $d_p = 60$ nm. Figure 4 shows a 2D slice in the xz -plane of two nanoparticle center-of-mass trajectories, highlighting two distinct classes of events. For these trajectories, the nanoparticle mobility was fixed at $\mu_{NP} = 0.8 \mu\text{m cm/V} \cdot \text{s}$. The trajectory drawn in black shows a particle fully translocate through the pore, which we refer to as a true “translocation event.” In contrast, the trajectory drawn in blue is representative of a class of event in which the particle passes near the entrance of the nanopore and causes a detectable change in the ionic current, but diffuses away from the nanopore without ever entering. Here, we refer to these events as “collisions,” although such events have also been called “bounce-off”⁵⁹ or “fly-by”¹⁶ elsewhere in the literature. Figure 4 also shows the relative change in the ionic current through the pore for different particle positions, represented by the red color map of the figure. For our simulations, we find that the current always decreases when a particle is within the pore, and for the values of nanoparticle diameter and pore size considered in the figure, the current decreases by as much as 40 – 60% for positions in the central portion of the channel.

To assess the uniformity of the translocation and collision events, we overlaid 500 independent events, as shown in Figure 5a. The events are characterized by the z -coordinate (i.e., position along the central axis of the nanopore) of the center-of-mass of a $d_{NP} = 40$ nm nanoparticle as a function of time for a configuration with $L_p = 60$ nm, and a particle mobility of $0.8 \mu\text{m cm/V} \cdot \text{s}$. The trajectories from translocation and collision events are depicted as black and blue lines, respectively. From the overlaid events, we observe that the slope of the black lines between $z = 300$ nm and $z = 200$ nm is relatively consistent between independent events, indicating that the particles move through the pore with compara-

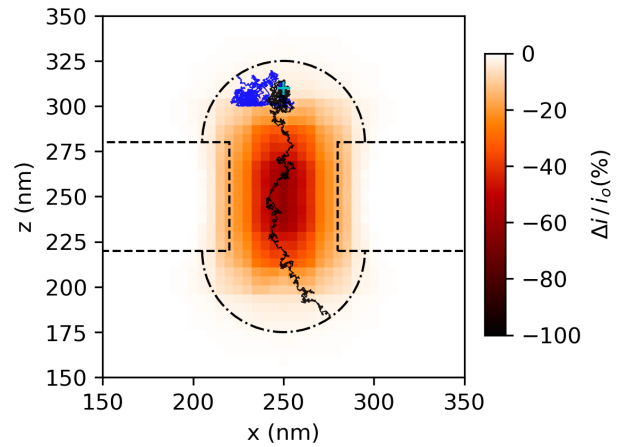


Fig. 4 Schematic of the configuration used to set the events. Dotted lines represent the membrane/pore location, whereas the dash-dotted lines indicate the boundaries where the trajectories are terminated. Projections of two trajectories are depicted in black (translocation) and blue (collision) lines. The color map shows the relative blockade caused by a $d_{NP} = 40$ nm particle positioned in each location. For these simulations, $d_p = L_p = 60$ nm.

ble velocities with some small variations due to Brownian motion. The dwell time of the nanoparticles is roughly on the order of $\tau = 50 \mu\text{s}$. Additionally, although we find that while most collision events consist of nanoparticles that diffuse in the vicinity of the entrance of the nanopore and only slightly disrupt the ionic current, occasionally nanoparticles enter the pore, as shown by those trajectories in the figure with a z -coordinate that is less than the sum of the top surface location and the radius of the nanoparticle ($z = 300$ nm). However, our simulations showed that the nanoparticles in such events do not enter more than about 10 – 15 nm into the pore (i.e., on the order of the radius of the nanoparticle). Experimentally, these events may be difficult to resolve due to their short duration and the relatively small amplitude of the blockade events, which we discuss in more detail below. Nevertheless, collision events have been detected experimentally.^{16,57}

Since the presence of collision events can affect interpretation of RPS measurements, they usually have to be removed from the analysis or at least correctly identified. For this reason, we next used DMC simulations to determine the relative frequency of true translocation events relative to all events. Figure 5b plots the translocation ratio (i.e., the ratio of translocation events relative to all events) as a function of nanoparticle mobility for nanoparticles with varying diameters and for three values of nanopore length. Circle, plus, and square points correspond to nanoparticles with diameters of $d_{NP} = 30, 40,$ and 50 nm. The colors of the points correspond to nanopores with lengths of $L_p = 20$ nm (blue), 60 nm (orange), and 100 nm (green). DMC simulations confirmed that for fixed d_{NP} and L_p , the translocation ratio increased from 20% to near 70% as the nanoparticle mobility increased from $\mu_{NP} = 0.4 \mu\text{m cm/V} \cdot \text{s}$ to $1.2 \mu\text{m cm/V} \cdot \text{s}$ for $d_{NP} = 50$ nm and $L_p = 100$ nm. In general, as either d_{NP} or L_p decreased, we observed that the fraction of translocation events increased, but for different reasons. As d_{NP} decreases, there is a

greater probability for the nanoparticle to be located in a lateral position in the nanopore that will allow it to fully pass across the membrane. In contrast, as L_P decreases, the probability that the nanoparticle will completely move through the channel increases since the path length it must diffuse across decreases.

Coupling our DMC simulations to PNP calculations of the ionic current with the MLP NN allowed us to obtain current traces for all of the 500 events shown in figure 5c. Figure 5c plots these current traces as a function of time, where the events were overlaid such that the minimum current in each event coincided with $t = 0 \mu\text{s}$. Similar current traces for the remaining values of d_{NP} , L_P , and μ_{NP} are presented in the ESI†. Translocation events collapsed into a well defined curve, with average blockades of $\Delta i \approx 3 \text{ nA}$. Because DMC simulated many different trajectories, the data in figure 2c also provide insight into the variability of the resistive pulses. However, our data only contains fluctuations from the Brownian motion of the nanoparticles, whereas experimental signals are also influenced by many other sources of noise.⁸³ Thus, we observe noise that is significantly lower than what might be seen experimentally. Nevertheless, from inspection of the width of the overlaid translocation events, we find that the magnitude of the pulse varied from about 1.25 nA to 3 nA. In contrast to the translocation events, while some collision events produced a noticeable decrease in the current of $\Delta i \approx 0.25 - 0.75 \text{ nA}$, other events did not produce an appreciable decrease in the current. In terms of dwell times, translocation events took on the order of $\tau = 50 \mu\text{s}$, as previous discussed, while collisions occurred at much shorter times as is evident from the much narrower pulse widths in figure 5c. As shown in previous work from White *et al.*, the short duration of the collision events combined with low-pass filters used in typical experiments means that experimentally, such collision events may be extremely attenuated or not detectable, depending on the dwell time, cutoff frequency of the low-pass filter, and the sampling rate of the amplifier.⁸⁴

To connect our DMC simulations to experimental measurements and extract quantitative trends, we fit each current trace independently with a Gaussian function to obtain the relative blockade $\Delta i/i_0$ and dwell time τ . A representative translocation event and fit is shown in figure 5d. While many software packages such as OpenNanopore⁸⁵, EventPro⁸⁶, and PyPore use the cumulative sum algorithm (CUSUM) to call events and subsequently fit them, we opted to use a fit to a Gaussian function because of its simplicity and the similarity in shape to our events. The event in figure 5d is a relatively short event of $\tau \approx 10 \mu\text{s}$, with a blockade amplitude of $\Delta i \approx 1.75 \text{ nA}$.

Figure 6 plots the relative blockade and dwell time obtained from Gaussian fits to the current traces for all values of particle diameter, pore length, and mobility that we simulated. In the top row, we have overlaid the results for all events, with the corresponding mean values and error from each configuration shown in the lower panels. The error was taken to be $\pm 2\sigma$, where σ is the standard deviation of the mean. Triangles, circles, and squares represent nanoparticles with diameters of $d_{NP} = 30, 40, \text{ and } 50 \text{ nm}$, respectively. The color of the points correspond to nanoparticle mobilities of $\mu_{NP} = 0.4 \mu\text{m cm/V} \cdot \text{s}$ (blue), $0.8 \mu\text{m cm/V} \cdot \text{s}$ (orange), and $1.2 \mu\text{m cm/V} \cdot \text{s}$ (green).

The compiled results provide guidance on experimental conditions for successful translocation measurements of nanoparticles in a few ways. First, we observe that for each particle size, there exist three populations of points corresponding to the three values of nanoparticle mobilities. However, we find that while the relative blockade each nanoparticle size is relatively constant (i.e., $\Delta i/i_0$ depends only on the size of the nanoparticle and not the mobility), there is overlap of the three populations of mobilities. This implies that for the values considered in this study, it may be difficult to resolve differences in nanoparticle mobilities by RPS measurements alone. Regardless, the results show that as the mobility increases, the variability in τ decreases, presumably due to faster, more directed motion of the nanoparticle through the nanopore as electrophoresis overcomes Brownian motion. This trend can be more quantitatively observed in the lower panels, where we observe the extent of the horizontal error bars decreases and the mean dwell time shifts to lower values as mobility increases. However, as the nanopore length increases from $L_P = 20 \text{ nm}$ to $L_P = 100 \text{ nm}$, we observe that the variability in dwell time increases due to the increased path length over which the nanoparticle must diffuse.

In contrast to trends with respect to discerning different values of nanoparticle mobility, our DMC simulations show that RPS measurements can easily distinguish between nanoparticles with different sizes independent of their mobilities. For the conditions studied here, we observe that the variability in the relative blockade is larger for the $d_{NP} > 30 \text{ nm}$ nanoparticles than for the $d_{NP} = 30 \text{ nm}$ particles, and that the variability slightly decreases as L_P increases. Thus, the optimal conditions for nanoparticle sensing should strike a balance between the higher resolution of the relative blockade that occurs for longer nanopores, and the larger translocation ratio that occurs as L_P decreases.

Finally, a common estimate of the relative blockade is obtained by assuming that the reduction in ionic current is due solely to the reduction in the cross sectional area of the nanopore due to the presence of the nanoparticle. Taking this approach, one finds that $\Delta i/i_0 = -(d_{NP}/d_P)^2$, which implies that for all values of L_P that we investigated, the expected relative blockade for $d_{NP} = 30 \text{ nm}$, 40 nm , and 50 nm nanoparticles, based solely on geometric effects, would be $\Delta i/i_0 = -0.25, 0.44, \text{ and } 0.69$, respectively, for a nanopore with diameter $d_P = 60 \text{ nm}$. Comparing these values to the data in the lower row of figure 6, we find that our DMC simulations predict relative blockades that can vary significantly from those obtained from a purely geometrical estimate. For instance, for the smallest nanoparticles we simulated ($d_{NP} = 30 \text{ nm}$), we find the relative blockade is smaller than the geometric estimate by approximately 5%. As the nanoparticle diameter increases, the relative blockade observed in our DMC simulations can be as much as 10 – 20% larger than the geometric estimate. The reason for this discrepancy may lie with the fact that the PNP calculations, which serve as the foundation for training the neural network, take into account the manner in which the presence of a nanoparticle in the nanopore changes the local electrostatic potential. Similarly, for charged nanoparticles (which we do not consider here), the PNP calculations and subsequently trained neural network offer a more detailed calculation of the expected

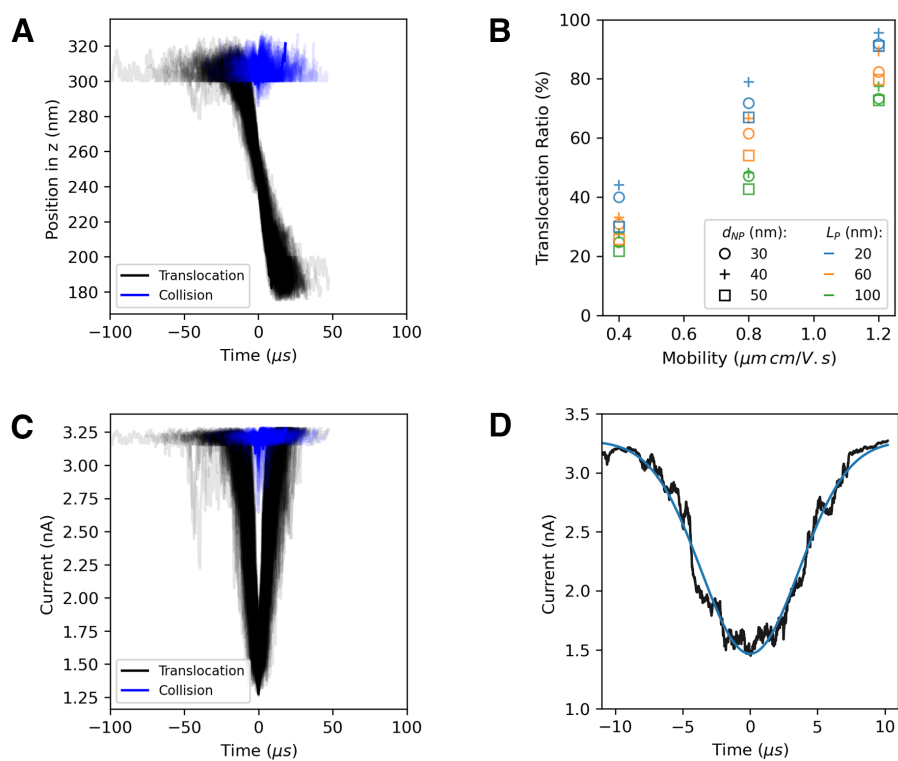


Fig. 5 (a) Position in the z direction as a function of time for 500 overlapped events for nanoparticles with $d_{NP} = 40$ nm and $\mu_{NP} = 0.8 \mu\text{m cm/V.s}$. Full translocation events are shown in black while collisions are shown in blue. (b) Translocation ratio as a function of nanoparticle mobility, diameter, and nanopore length. (c) Current as function of time for 500 overlapped events simulating nanoparticles with $d_{NP} = 40$ nm and $\mu_{NP} = 0.8 \mu\text{m cm/V.s}$. Full translocation events in black and collisions events in blue. (d) Representative current trace from a single translocation event of a $d_{NP} = 40$ nm nanoparticle with mobility of $\mu_{NP} = 0.8 \mu\text{m cm/V.s}$. A Gaussian fit (blue line) was used to extract the dwell time and current blockade. The nanopore diameter was fixed at $d_p = 60$ nm for all simulations.

current. Finally, while the geometrical estimate does depend on L_P , the results in figure 6 clearly show that as L_P increases, both the relative blockade and its variance decrease.

3.3 Comparison to Experiments

To assess whether the trends observed from our DMC simulations are representative of real translocation processes, we performed RPS measurements to track Au nanosphere ($d_{NP} = 30$ nm) translocation. Prior work by others,^{3,4} as well as our own RPS measurements, has shown that citrate-coated Au nanoparticles produce a positive relative blockade (*i.e.*, conductive pulses) while they reside within a nanopore. This has been attributed to the effects of the electrical double layers of the nanoparticles and the nanopores that lead to an increase in the conductivity. To avoid such effects and more closely match our DMC simulations which did not account for the charge of the nanoparticle or the nanopore, we focused on CTAB-coated Au nanospheres that were dispersed in a 500 mM KCl solution to screen as much charge as possible. Whereas citrate-coated Au nanoparticles can only disperse at concentrations of KCl up to about 1.5 mM, CTAB-coated nanoparticles can tolerate KCl concentrations up to at least 500 mM. Finally, to amplify the experimental signal, we applied a bias of 200 mV rather than 100 mV. However, since we characterize the translocation events by the *relative* blockade, this does not affect our comparison to simulations.

Shown in figure 7 are (a) several seconds of ionic current measurements, showing resistive pulses that correspond to the translocation of $d_{NP} = 30$ nm nanoparticles through a nanopore ($d_P = 80$ nm, $L_P = 100$ nm) etched into a SiO₂-supported SiN_x membrane, and (b) selected translocation events shown at a magnified time scale. The final bandwidth of the measurement after applying a low-pass filter was $\Delta f = 20$ kHz. We observe from figure 7a that the translocation pulses are on the order of $\Delta i \approx 0.5$ nA. From the magnified data in figure 7b, we see that presence what may be true translocation events, such as the one shown in black, but that translocation events appear alongside what may be collisions, such as the short red pulses towards the right side of the red trace.

The data were analyzed using Pypore, developed by the Drndić Laboratory, and events were identified using the CUSUM algorithm. The current trace contained 164 events which were fit to a square profile to obtain the average dwell time τ and $\Delta i/i_0$. Our measurements found $\tau = 31 \mu\text{s}$ and $\Delta i/i_0 = -0.10$. Experimentally, our bandwidth $\Delta f = 20$ kHz presents challenges for resolving events that occur for $\tau < 1/\Delta f \approx 50 \mu\text{s}$. Events shorter than $50 \mu\text{s}$ may not be detected, and those events which are may have attenuated or distorted signatures. Although the bandwidth of our measurements will lead to attenuation of events that occur for $\tau < 50 \mu\text{s}$, we chose not to exclude shorter events and our average values are obtained from all events. This may lead to a slightly lower value for $\Delta i/i_0$ relative to the true value. However, since τ is close to the limit of $50 \mu\text{s}$, we believe that this effect may be small.

Figure 7c plots our experimental point as a black diamond, while the orange triangle point shows the results for a DMC sim-

ulation using the same experimental conditions and $\mu_{NP} = 0.25 \mu\text{m cm/V} \cdot \text{s}$. We observe good agreement between the predictions of τ and $\Delta i/i_0$ from our DMC simulations and the experimental measurements, although we observe a slightly more disperse response for τ in the simulated results as well as a higher dispersion of the $\Delta i/i_0$ in the experiment. We speculate that the origin of these differences may be due to the fact that experimental measurements miss shorter pulses which leads to a decreased variance in τ compared to the simulations. At the same time, the nanoparticles used in our experiments possess inherent polydispersity in their dimensions, which in turn leads to a larger variance in $\Delta i/i_0$ as compared to the simulations.

4 Summary

Time-resolved trajectories that are consistent with the drift-diffusion process were simulated simultaneously with the associated current responses of these trajectories during translocation using a combination of Dynamic Monte Carlo (DMC) simulations, Poisson-Nernst-Planck (PNP) calculations, and a Multilayer Perceptron Neural Network (MLP NN) to connect the DMC to PNP results. Our simulations found that uncharged nanoparticles would produce resistive spikes with magnitudes related to the size of the particles. The resistive spikes observed in our simulations were consistent with those measured experimentally by resistive pulse sensing (RPS). Simultaneous simulation of nanoparticle transport through the nanopore and the associated ionic current response allowed us to not only simulate hundreds of independent nanoparticle trajectories, but also to identify optimal conditions for determining nanoparticle size and mobility. For instance, our results demonstrate that using longer nanopores leads to more uniform translocation events which, in turn, results the ability to better resolve differences in nanoparticle size.

Despite the successes of this approach, we note that several simplifications were made in this study. First, the fluid is not explicitly modeled (*e.g.*, by solving the Navier-Stokes equation), which neglects the effect of hydrodynamic interactions on nanoparticle transport. In addition, the membrane and nanoparticle surfaces were treated as uncharged within our PNP calculations, which in conjunction to the lack of hydrodynamics, neglects the effect of electro-osmotic flow. However, because of the relatively high ionic strength of the electrolyte in our experiments, a significant degree of charge screening occurs which supports our use of this simplification. Finally, the spatial resolution of the PNP calculations is somewhat limited, which could be improved in order to simulate charged surfaces. Moving forward, the use multi-physics software with adaptive meshing can address these limitations.

Although we utilized a MLP NN to make simultaneous simulation of nanoparticle transport and ionic current possible, the mapping of the electrostatic potential into the DMC code could have been done using an interpolation scheme, similar to the approach we took for calculating the current. In such an approach, the results of PNP simulations for the electrostatic potential at each grid position can be stored onto data arrays to be interpolated for a given position of the particle. However, we believe the machine learning approach has the potential to be further devel-

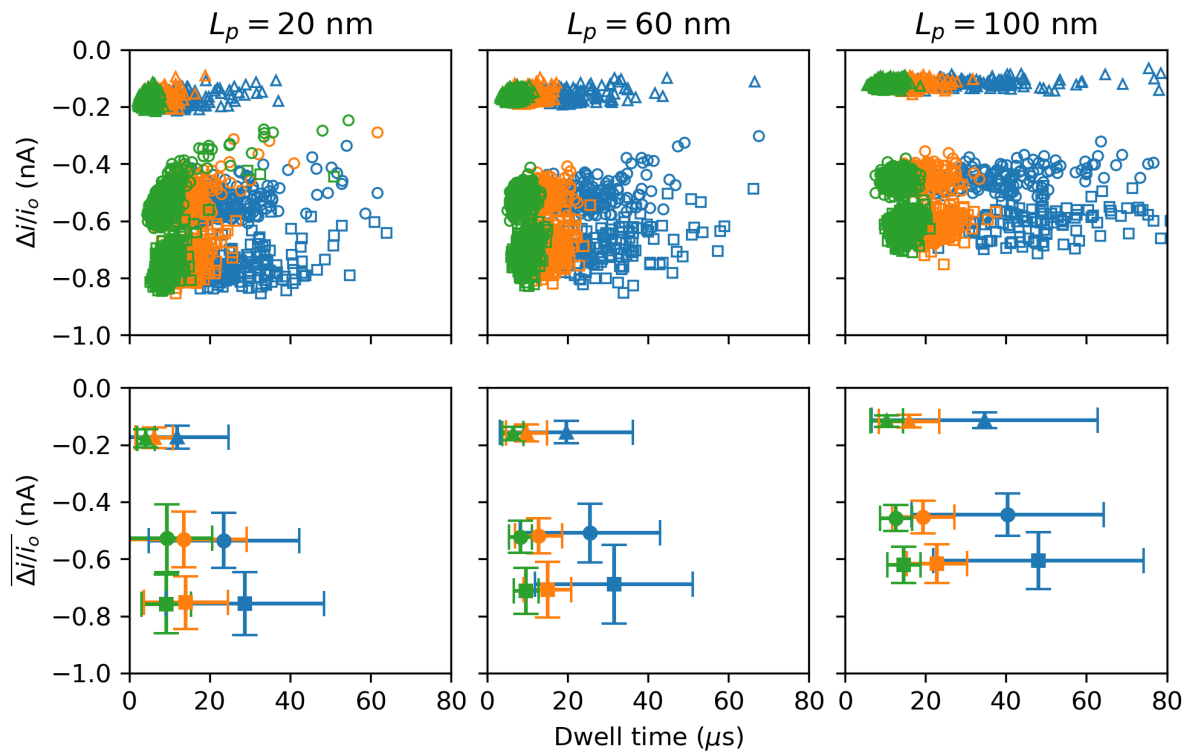


Fig. 6 Summary of DMC simulation results for all nanoparticle and nanopore combinations. The top row plots the relative blockade versus dwell time for all events at a fixed nanopore diameter of $d_p = 60$ nm and nanopore length of (left to right) $L_p = 20$ nm, 60 nm, and 100 nm. The lower row displays only the mean values. The symbol type designates nanoparticle diameters of $d_{NP} = 30$ nm (triangles), 40 nm (circles), and 50 nm (squares). Nanoparticle mobilities, designated by the symbol color, correspond to $\mu_{NP} = 0.4$ μ mcm/V·s (blue), 0.8 μ mcm/V·s (orange) and 1.2 μ mcm/V·s. Error bars represent two standard deviations from the mean value.

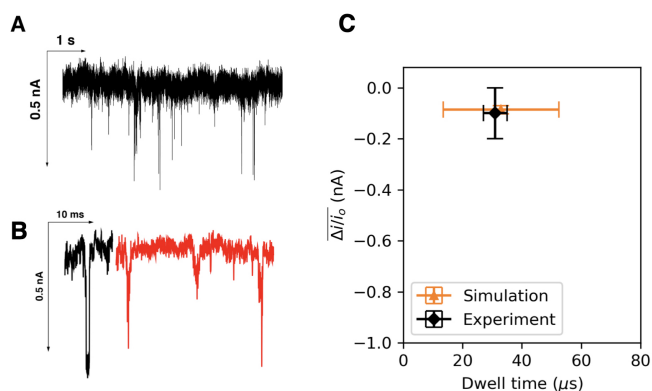


Fig. 7 Experimental RPS measurements of $d_{NP} = 30$ nm CTAB-coated Au nanoparticles. (a) Ionic current as a function of time over an interval of approximately 10 s. The large downward spikes in the current are translocation events which are roughly on the order of 0.5 nA. (b) Concatenated translocation and collision events extracted from two separate recordings (represented as black and red traces). Collision events can be observed as small pulses while true translocation events occur as large spikes. (c) Comparison between experimental RPS measurements (black point) and a DMC simulation with matching parameters of $d_{NP} = 30$ nm and $d_p = 80$ nm.

oped considering the recent growth of the field. For example, the network architecture can be greatly improved by hyperparameter optimization⁸⁷, allowing for better prediction of the electrostatic potential with the same computational cost. In addition, classes of neural networks other than MLPs, such as convolutional neural networks, can also be investigated.

Finally, we envision the possibility of using physics-informed neural networks^{88–90}, where constraints applied into the network training can result in greater generalization from a small data set.

Notwithstanding its limitations, our approach combining Machine Learning with DMC proved to be flexible enough to simulate several configurations after the initial data generation and training step. The MLP NN was able to capture the voltage profile around and inside the pore calculated by PNP. The prediction performance of the neural network was also investigated, depending on the architecture of the model. The strategy of employing a neural network was successful for quickly estimating the electrostatic potential as the nanoparticle changed locations, allowing us to simulate many trajectories. The relative blockade and dwell time results from many trajectories of particles with different sizes and mobilities showed a significant overlap of the populations, indicating the existence of a limit of discrimination for particles with similar characteristics. This limit arises due to the Brownian motion of the nanoparticles. Our results also show that although longer pores lead to more variability in dwell time, higher values of L_p enhanced the differences in the mean value, with the net effect of helping with discrimination of particles having similar sizes and different values of mobility. Interestingly, longer pores *reduced* the variability of the values of relative blockade, also helping with discrimination of particles with distinct sizes. Looking forwards the future, we expect that our combined DMC/MLP NN approach to studying nanoparticle translocation can be further developed in order to achieve increasingly realistic translocation

simulations to further the development of nanopore sensing of nanoparticles and related materials.

Conflicts of interest

There are no conflicts to declare.

Acknowledgements

This work made use of the High Performance Computing Resource in the Core Facility for Advanced Research Computing at Case Western Reserve University. MJAH acknowledges support from a National Science Foundation CAREER Award from the Polymers program (DMR-1651002). This study was financed in part by the Coordenação de Aperfeiçoamento de Pessoal de Nível Superior – Brasil (CAPES) – Finance Code 001.

Notes and references

- 1 J. R. Werber, C. O. Osuji and M. Elimelech, *Nature Reviews Materials*, 2016, **1**, year.
- 2 T. Wei, A. Kikuchi, Y. Moriyasu, N. Suzuki, T. Shimizu, K. Hagiwara, H. Chen, M. Takahashi, T. Ichiki-Uehara and T. Omura, *Journal of Virology*, 2006, **80**, 8593–8602.
- 3 E. Weatherall and G. R. Willmott, *The Journal of Physical Chemistry B*, 2015, **119**, 5328–5335.
- 4 G. Goyal, K. J. Freedman and M. J. Kim, *Analytical chemistry*, 2013, **85**, 8180–8187.
- 5 K. E. Venta, M. B. Zanjani, X. Ye, G. Danda, C. B. Murray, J. R. Lukes and M. Drndić, *Nano Letters*, 2014, **14**, 5358–5364.
- 6 R. Maugi, P. Hauer, J. Bowen, E. Ashman, E. Hunsicker and M. Platt, *Nanoscale*, 2020, **12**, 262–270.
- 7 S. Kishimoto, S. Murayama, M. Tsutsui and M. Taniguchi, *ACS Sensors*, 2020, **5**, 1597–1603.
- 8 X. L. Nie, H. L. Liu, Z. Q. Pan, S. A. Ahmed, Q. Shen, J. M. Yang, J. B. Pan, J. Pang, C. Y. Li, X. H. Xia and K. Wang, *Chemical Communications*, 2019, **55**, 6397–6400.
- 9 J. S. Lee, J. Saharia, Y. M. D. Bandara, B. I. Karawdeniya, G. Goyal, A. Darvish, Q. Wang, M. J. Kim and M. J. Kim, *Electrophoresis*, 2019, **40**, 1337–1344.
- 10 A. D. Grabarek, D. Weinbuch, W. Jiskoot and A. Hawe, *Journal of Pharmaceutical Sciences*, 2019, **108**, 563–573.
- 11 O. Liot, M. Socol, L. Garcia, J. Thiéry, A. Figarol, A. F. Mingotaud and P. Joseph, *Journal of Physics: Condensed Matter*, 2018, **30**, 234001.
- 12 M. Tsutsui, K. Yokota, T. Nakada, A. Arima, W. Tonomura, M. Taniguchi, T. Washio and T. Kawai, *ACS Sensors*, 2018, **3**, 2693–2701.
- 13 J. S. Lee, B. Peng, A. C. Sabuncu, S. Nam, C. W. Ahn, M. J. Kim and M. J. Kim, *Electrophoresis*, 2018, **39**, 833–843.
- 14 S. Ryuzaki, M. Tsutsui, Y. He, K. Yokota, A. Arima, T. Morikawa, M. Taniguchi and T. Kawai, *Nanotechnology*, 2017, **28**, 155501.
- 15 E. L. Blundell, R. Vogel and M. Platt, *Langmuir*, 2016, **32**, 1082–1090.
- 16 M. Tsutsui, Y. He, K. Yokota, A. Arima, S. Hongo, M. Taniguchi, T. Washio and T. Kawai, *ACS Nano*, 2016, **10**, 803–809.

- 17 S. Tan, L. Wang, H. Liu, H. Wu and Q. Liu, *Nanoscale Research Letters*, 2016, **11**, 1–10.
- 18 M. A. Edwards, S. R. German, J. E. Dick, A. J. Bard and H. S. White, *ACS Nano*, 2015, **9**, 12274–12282.
- 19 W. J. Lan, C. Kubeil, J. W. Xiong, A. Bund and H. S. White, *Journal of Physical Chemistry C*, 2014, **118**, 2726–2734.
- 20 P. Terejanski, I. Makra, P. Furjes and R. E. Gyurcsanyi, *Analytical Chemistry*, 2014, **86**, 4688–4697.
- 21 D. Kozak, W. Anderson, R. Vogel, S. Chen, F. Antaw and M. Trau, *ACS Nano*, 2012, **6**, 6990–6997.
- 22 G. S. Roberts, S. Yu, Q. Zeng, L. C. Chan, W. Anderson, A. H. Colby, M. W. Grinstaff, S. Reid and R. Vogel, *Biosensors and Bioelectronics*, 2012, **31**, 17–25.
- 23 M. Pevarnik, K. Healy, M. E. Toimil-Molares, A. Morrison, S. E. Letant and Z. S. Siwy, *ACS Nano*, 2012, **6**, 7295–7302.
- 24 N. Arjmandi, W. Van Roy, L. Lagae and G. Borghs, *Analytical Chemistry*, 2012, **84**, 8490–8496.
- 25 W. J. Lan and H. S. White, *ACS Nano*, 2012, **6**, 1757–1765.
- 26 R. Vogel, W. Anderson, J. Eldridge, B. Glossop and G. Willmott, *Analytical Chemistry*, 2012, **84**, 3125–3131.
- 27 T. Z. Jubery, A. S. Prabhu, M. J. Kim and P. Dutta, *Electrophoresis*, 2012, **33**, 325–333.
- 28 W. J. Lan, D. A. Holden, J. Liu and H. S. White, *Journal of Physical Chemistry C*, 2011, **115**, 18445–18452.
- 29 R. Vogel, G. Willmott, D. Kozak, G. S. Roberts, W. Anderson, L. Groenewegen, B. Glossop, A. Barnett, A. Turner and M. Trau, *Analytical Chemistry*, 2011, **83**, 3499–3506.
- 30 W. J. Lan, D. A. Holden, B. Zhang and H. S. White, *Analytical Chemistry*, 2011, **83**, 3840–3847.
- 31 A. S. Prabhu, T. Z. N. Jubery, K. J. Freedman, R. Mulero, P. Dutta and M. J. Kim, *Journal of Physics: Condensed Matter*, 2010, **22**, 454107.
- 32 G. R. Willmott, S. S. Yu and R. Vogel, *ICONN 2010 - Proceedings of the 2010 International Conference on Nanoscience and Nanotechnology*, 2010, 128–131.
- 33 G. R. Willmott, R. Vogel, S. S. Yu, L. G. Groenewegen, G. S. Roberts, D. Kozak, W. Anderson and M. Trau, *Journal of Physics Condensed Matter*, 2010, **22**, year.
- 34 T. Ito, L. Sun, M. A. Bevan and R. M. Crooks, *Langmuir*, 2004, **20**, 6940–6945.
- 35 L. Bacri, A. G. Oukhaled, B. Schiedt, G. Patriarche, E. Bourhis, J. Gierak, J. Pelta and L. Auvray, *Journal of Physical Chemistry B*, 2011, **115**, 2890–2898.
- 36 A. Sikora, A. G. Shard and C. Minelli, *Langmuir*, 2016, **32**, 2216–2224.
- 37 R. Akahori, K. Esashika, I. Yanagi and T. Saiki, *Japanese Journal of Applied Physics*, 2020, **59**, 107001.
- 38 D. Coglitore, P. E. Coulon, J. M. Janot and S. Balme, *Materials*, 2019, **12**, 1–11.
- 39 F. He, B. Yin, W. Xie, L. Yu, S. Tong, L. Liang and D. Wang, *Conference Program Digest - 7th International Conference on Manipulation, Manufacturing and Measurement on the Nanoscale, IEEE 3M-NANO 2017*, 2018, **2018-Janua**, 388–391.
- 40 Y. Kim, M. E. Lobatto, T. Kawahara, B. L. Chung, A. J. Mieszawska, B. L. Sanchez-Gaytan, F. Fay, M. L. Senders, C. Calcagno, J. Becraft, M. T. Saung, R. E. Gordon, E. S. Stroes, M. Ma, O. C. Farokhzad, Z. A. Fayad, W. J. Mulder and R. Langer, *Proceedings of the National Academy of Sciences of the United States of America*, 2014, **111**, 1078–1083.
- 41 K. E. Venta, M. B. Zanjani, X. Ye, G. Danda, C. B. Murray, J. R. Lukes and M. Drndic, *Nano Letters*, 2014, **14**, 5358–5364.
- 42 Y. Wang, K. Kececi, M. V. Mirkin, V. Mani, N. Sardesai and J. F. Rusling, *Chemical Science*, 2013, **4**, 655–663.
- 43 F. He, L. Liang, S. Zhou, W. Xie, S. He, Y. Wang, C. Tlili, S. Tong and D. Wang, *Langmuir*, 2018, **34**, 14825–14833.
- 44 M. Platt, G. R. Willmott and G. U. Lee, *Small*, 2012, **8**, 2436–2444.
- 45 W. Si, J. Sha, Q. Sun, Z. He, L. Wu, C. Chen, S. Yu and Y. Chen, *The Analyst*, 2020, **145**, 1657–1666.
- 46 R. E. Lane, D. Korbie, W. Anderson, R. Vaidyanathan and M. Trau, *Scientific Reports*, 2015, **5**, 1–7.
- 47 A. Darvish, G. Goyal, R. Aneja, R. V. Sundaram, K. Lee, C. W. Ahn, K. B. Kim, P. M. Vlahovska and M. J. Kim, *Nanoscale*, 2016, **8**, 14420–14431.
- 48 F. A. Coumans, E. van der Pol, A. N. Boing, N. Hajji, G. Sturk, T. G. van Leeuwen and R. Nieuwland, *Journal of Extracellular Vesicles*, 2014, **3**, 1–8.
- 49 D. A. Holden, J. J. Watkins and H. S. White, *Langmuir*, 2012, **28**, 7572–7577.
- 50 A. Arima, M. Tsutsui, I. H. Harlisa, T. Yoshida, M. Tanaka, K. Yokota, W. Tonomura, M. Taniguchi, M. Okochi, T. Washio and T. Kawai, *Scientific Reports*, 2018, **8**, year.
- 51 R. W. DeBlois, C. P. Bean and R. K. Wesley, *Journal of Colloid And Interface Science*, 1977, **61**, 323–335.
- 52 Z. D. Harms, K. B. Mogensen, P. S. Nunes, K. Zhou, B. W. Hildenbrand, I. Mitra, Z. Tan, A. Zlotnick, J. P. Kutter and S. C. Jacobson, *Analytical Chemistry*, 2011, **83**, 9573–9578.
- 53 H. Wu, Y. Chen, Q. Zhou, R. Wang, B. Xia, D. Ma, K. Luo and Q. Liu, *Analytical Chemistry*, 2016, **88**, 2502–2510.
- 54 J. L. Fraikin, T. Teesalu, C. M. McKenney, E. Ruoslahti and A. N. Cleland, *Nature Nanotechnology*, 2011, **6**, 308–313.
- 55 J. D. Uram, K. Ke, A. J. Hunt and M. Mayer, *Small*, 2006, **2**, 967–972.
- 56 A. Darvish, G. Goyal and M. Kim, *Advances in Global Health through Sensing Technologies 2015*, 2015, **9490**, 94900M.
- 57 A. McMullen, H. W. de Haan, J. X. Tang and D. Stein, *Nature Communications*, 2014, **5**, year.
- 58 A. J. McMullen, J. X. Tang and D. Stein, *ACS Nano*, 2017, **11**, 11669–11677.
- 59 W. R. Lenart, W. Kong, W. C. Oltjen and M. J. Hore, *Journal of Materials Chemistry B*, 2019, **7**, 6428–6437.
- 60 T. G. Souza, V. S. Ciminelli and N. D. Mohallem, *Journal of Physics: Conference Series*, 2016, **733**, 1–5.
- 61 J. A. Somerville, G. R. Willmott, J. Eldridge, M. Griffiths and K. M. McGrath, *Journal of Colloid and Interface Science*, 2013, **394**, 243–251.
- 62 M. Pevarnik, M. Schiel, K. Yoshimatsu, I. V. Vlassioux, J. S.

- Kwon, K. J. Shea and Z. S. Siwy, *ACS Nano*, 2013, **7**, 3720–3728.
- 63 D. A. Holden, G. Hendrickson, L. A. Lyon and H. S. White, *Journal of Physical Chemistry C*, 2011, **115**, 2999–3004.
- 64 D. J. Niedzwiecki, Y.-C. Chou, Z. Xia, F. Thei and M. Drndić, *Review of Scientific Instruments*, 2020, **91**, 031301.
- 65 M. Taniguchi, *ACS Omega*, 2020, **5**, 959–964.
- 66 L. Qiao and G. W. Slater, *Journal of Chemical Physics*, 2020, **152**, 1–6.
- 67 A. McMullen, H. W. De Haan, J. X. Tang and D. Stein, *Physical Review Letters*, 2018, **120**, 78101.
- 68 L. Qiao, M. Ignacio and G. W. Slater, *Journal of Chemical Physics*, 2019, **151**, 1–11.
- 69 E. E. Michaelides, *International Journal of Heat and Mass Transfer*, 2017, **114**, 607–612.
- 70 M. Kuron, G. Rempfer, F. Schornbaum, M. Bauer, C. Godenschwager, C. Holm and J. de Graaf, *The Journal of Chemical Physics*, 2016, **145**, 214102.
- 71 S. Reboux, F. Capuani, N. González-Segredo and D. Frenkel, *Journal of Chemical Theory and Computation*, 2006, **2**, 495–503.
- 72 Z. Qin, J. Zhe and G.-X. Wang, *Measurement Science and Technology*, 2011, **22**, 045804.
- 73 Y. W. Liu, S. Pennathur and C. D. Meinhart, *Physics of Fluids*, 2014, **26**, 1–12.
- 74 S. Qian, A. Wang and J. K. Afonien, *Journal of Colloid and Interface Science*, 2006, **303**, 579–592.
- 75 Y. Zhang, M. A. Edwards, S. R. German and H. S. White, *Journal of Physical Chemistry C*, 2016, **120**, 20781–20788.
- 76 W. J. Lan, D. A. Holden, B. Zhang and H. S. White, *Analytical Chemistry*, 2011, **83**, 3840–3847.
- 77 J. Slotboom and H. De Graaff, *Solid-State Electronics*, 1976, **19**, 857–862.
- 78 K. Kikuchi, M. Yoshida, T. Maekawa and H. Watanabe, 1991, **185**, 335–338.
- 79 A. Patti and A. Cuetos, *Physical Review E - Statistical, Nonlinear, and Soft Matter Physics*, 2012, **86**, 1–9.
- 80 A. Cuetos and A. Patti, *Physical Review E*, 2015, **92**, 022302.
- 81 C. Wen, Z. Zhang and S.-L. Zhang, *ACS Sensors*, 2017, **2**, 1523–1530.
- 82 L. van Oeffelen, W. V. Roy, D. Charlier, L. Lagae and G. Borghs, *Nanopores for Bioanalytical Applications*, Royal Society of Chemistry, 2012, pp. 51–56.
- 83 S. Liang, F. Xiang, Z. Tang, R. Nouri, X. He, M. Dong and W. Guan, *Nanotechnology and Precision Engineering*, 2020, **3**, 9–17.
- 84 D. A. Robinson, M. A. Edwards, H. Ren and H. S. White, *Chem-ElectroChem*, 2018, **5**, 3059–3067.
- 85 C. Raillon, P. Granjon, M. Graf, L. J. Steinbock and A. Radenovic, *Nanoscale*, 2012, **4**, 4916.
- 86 Y. M. N. D. Y. Bandara, J. Saharia, B. I. Karawdeniya, P. Kluth and M. J. Kim, *Analytical Chemistry*, 2021, **93**, 11710–11718.
- 87 L. Yang and A. Shami, *Neurocomputing*, 2020, **415**, 295–316.
- 88 T. Beucler, M. Pritchard, S. Rasp, J. Ott, P. Baldi and P. Gentine, *Physical Review Letters*, 2021, **126**, 98302.
- 89 G. E. Karniadakis, I. G. Kevrekidis, L. Lu, P. Perdikaris, S. Wang and L. Yang, *Nature Reviews Physics*, 2021, **3**, 422–440.
- 90 M. Raissi, P. Perdikaris and G. E. Karniadakis, *Journal of Computational Physics*, 2019, **378**, 686–707.